J Nanostruct 16(3): 3706-3717, Summer 2026

RESEARCH PAPER

Synthesis, Spectroscopic and Nano-Structural Characterization, Molecular Docking, and Corrosion Inhibition Studies of Novel Nano-Schiff Base Ligands Derived from 2-Aminobenzothiazole and Substituted Salicylaldehyde

Lina Abdullah Naser [1*], *Ali Fares Al-Ghazzi* [2], *Rasha Shakir Mahmood* [3]

[1] *Department of Nursing Technology, Technical Institute, Southern Technical University, Nasiriyah, Iraq*

[2] *Ministry of Education - General Directorate of Education of Dhi Qar, Nasiriyah, Iraq*

[3] *Department of Chemistry, College of Science, University of Misan, Maysan, Iraq*

ARTICLE INFO

Article History:
Received 25 March 2026
Accepted 24 June 2026
Published 01 July 2026

Keywords:
2-Aminobenzothiazole
Corrosion inhibition
Nano-organic inhibitors
Nano-Schiff base ligands
Nanostructured organic compounds

ABSTRACT

Two novel nano-Schiff base ligands, (E)-2-((benzo[d]thiazol-2-ylimino)methyl)phenol (nano-HL1) and (E)-4-bromo-2-((benzo[d] thiazol-2-ylimino) methyl) phenol (nano-HL2), were synthesised by condensing 2-aminobenzothiazole with 2-hydroxybenzaldehyde and 5-bromosalicylaldehyde, respectively, and were obtained as nanostructured solids with crystallite sizes well below 30 nm. FTIR, XRD, and FESEM characterised their structures and morphologies. FTIR bands at 1616 and 1621 cm-1 for nano-HL1 and nano-HL2 verified azomethine (C=N) production. Both ligands were semicrystalline, however nano-HL2 had significantly higher crystallinity, probably due to the bromine substituent. FESEM showed nanoscale rod-like and spherical aggregates. AutoDock Vina molecular docking against human serum albumin (HSA, PDB: 1AO6) showed higher binding for nano-HL2 (-8.7 kcal/mol) than nano-HL1 (-7.9 kcal/mol), likely due to additional halogen bonding interactions. Mild steel corrosion inhibition in 1.0 M HCl was assessed by weight loss and potentiodynamic polarisation. The maximum inhibition efficiency of nano-HL2 reached 94.2% at 500 ppm and 303 K, while nano-HL1 was 89.6%. Adsorption of both ligands on the steel surface followed the Langmuir isotherm. These nano-Schiff base ligands with their nanoscale crystallite domains, nanostructured surface morphology and pronounced surface activity—are promising candidates as nano-organic corrosion inhibitors and potential bioactive nanomaterials.

How to cite this article
Abdullah Naser L., Al-Ghazzi A., Shakir Mahmood R. Synthesis, Spectroscopic and Nano-Structural Characterization, Molecular Docking, and Corrosion Inhibition Studies of Novel Nano-Schiff Base Ligands Derived from 2-Aminobenzothiazole and Substituted Salicylaldehyde. J Nanostruct, 2026; 16(3):3706-3717. DOI: 10.22052/JNS.2026.03.059

INTRODUCTION

Schiff bases are one of the most studied organic ligands in coordination chemistry [1,2]. They are produced by condensation reactions between primary amines and carbonyl compounds. The azomethine (C=N) group and donor atoms like nitrogen, oxygen, and sulphur give them flexible coordination properties that make them valuable in catalysis, materials science, biological, and medicinal applications [3,4]. Schiff bases from heterocyclic amines, notably benzothiazole-based derivatives, have garnered attention in the last two

* *Corresponding Author Email: lina.abdullah@stu.edu.iq*

decades due to their biological activity and ability to form stable chelates with transition metals [5,6,7,8]. Mild steel corrosion in acidic media is an important economic problem in many industrial processes such as oil refining, chemical production and acid pickling [9,10]. One of the most successful and practical techniques to decrease corrosion-related flaws is the adsorption of organic inhibitors onto metal surfaces to produce a protective barrier [11]. Schiff bases have been extensively explored as inhibitors because of their large molecular size, lone-pair electrons on heteroatoms, and pi-electron systems, which allow strong adsorption on metal surfaces [12,13]. Recent studies have demonstrated that Schiff bases containing benzothiazole moieties are frequently superior inhibitors than simpler compounds because of the electron-donating sulphur and nitrogen atoms present in the heterocyclic ring [14,15]. Molecular docking, a strong computational method for predicting small molecule binding affinity and interaction patterns with target proteins, has also provided useful insights into possible pharmaceutical applications [16,17]. The structure-activity relationships governing Schiff base performance can be fully understood by integrating experimental synthesis, spectroscopic characterisation, theoretical docking studies, and corrosion inhibition evaluation [18]. In recent years, the design of nano-organic compounds and nanostructured Schiff bases has emerged as a particularly active research direction, because reducing the crystallite domains of organic ligands to the sub-100 nm range substantially increases their effective surface area, enhances their adsorption capacity on metal substrates, and improves their accessibility to biological targets. Within this context, the present study synthesises two nano-Schiff base ligands from 2-aminobenzothiazole condensed with salicylaldehyde derivatives, characterises them at the nanoscale using FTIR, XRD and FESEM (yielding nanoscale crystallite sizes of 22–28 nm and particle dimensions well below 100 nm), determines their molecular docking behaviour against human serum albumin, and tests their corrosion inhibition potential on mild steel in hydrochloric acid.

MATERIALS AND METHODS

Chemicals and Reagents

All chemicals and solvents used in this work were of analytical reagent grade and were employed without any additional purification. 2-Aminobenzothiazole (98%), 2-hydroxybenzaldehyde (salicylaldehyde, 99%), 5-bromosalicylaldehyde (98%), absolute ethanol, glacial acetic acid, and hydrochloric acid (37%) were obtained from Sigma-Aldrich and Merck. Mild steel specimens with the following composition: C 0.18%, Mn 0.35%, Si 0.17%, P 0.025%, S 0.023%, and the remainder Fe, were supplied by a local source and cut into coupons measuring 2.5 cm x 2.0 cm x 0.1 cm. Before the experiments, the steel coupons were mechanically polished using successive grades of silicon carbide emery paper (320, 600, 800, and 1200 grit), then degreased with acetone, washed with distilled water, and finally dried under ambient conditions [19].

Synthesis of Schiff Base Ligands

The two Schiff base ligands were prepared following a general procedure adapted from previous literature with some modifications [20,21]. For the synthesis of nano-HL1, an equimolar mixture of 2-aminobenzothiazole (1.50 g, 10 mmol) and 2-hydroxybenzaldehyde (1.22 g, 10 mmol) was dissolved in 30 mL of absolute ethanol with 2-3 drops of glacial acetic acid as a catalyst. The reaction mixture was heated under reflux at 78 degrees Celsius for approximately 4 hours with continuous stirring. The progress of the reaction was monitored by thin-layer chromatography (TLC) using ethyl acetate/hexane (3:7 v/v) as the eluent. Upon completion, the resulting bright yellow solution was allowed to cool to room temperature, and the precipitated solid was collected by vacuum filtration, washed thoroughly with cold ethanol, and recrystallized from hot ethanol to afford nano-HL1 as pale yellow crystals. Yield: 82%. Melting point: 178-180 degrees Celsius.

nano-HL2 was synthesized in an analogous manner by reacting 2-aminobenzothiazole (1.50 g, 10 mmol) with 5-bromosalicylaldehyde (2.01 g, 10 mmol) under identical reflux conditions. The product was obtained as light orange crystals after recrystallization. Yield: 78%. Melting point: 195-197 degrees Celsius. Both products were dried in a vacuum desiccator and stored in amber vials until further analysis.

Characterization Techniques

Fourier-transform infrared spectra were recorded on a Shimadzu FTIR-8400S

spectrophotometer in the range of 4000-400 cm^{-1} using KBr pellets. X-ray diffraction measurements were performed on a Rigaku MiniFlex 600 diffractometer equipped with Cu-Ka radiation (lambda = 1.5406 angstroms) operating at 40 kV and 15 mA, scanning over a 2-theta range of 10 to 80 degrees at a rate of 2 degrees per minute. The surface morphology and nano-structural features were examined using a TESCAN MIRA3 field-emission scanning electron microscope operated at an accelerating voltage of 15 kV. Samples for FESEM analysis were sputter-coated with a thin gold layer to enhance conductivity [22,23].

Molecular Docking Studies

Molecular docking calculations were carried out using AutoDock Vina software (version 1.1.2) [24]. The three-dimensional crystal structure of human serum albumin (HSA) was retrieved from the RCSB Protein Data Bank (PDB ID: 1AO6) at a resolution of 2.5 angstroms [25]. Prior to docking, the protein structure was prepared by removing water molecules, co-crystallized ligands, and adding polar hydrogen atoms using AutoDock Tools (ADT) v1.5.7. The three-dimensional structures of nano-HL1 and nano-HL2 were built and energy-minimized using Gaussian 09W at the B3LYP/6-31G(d,p) level of density functional theory (DFT) [26]. Gasteiger charges were computed for both the protein and the ligands. A grid box centred on the Sudlow site I binding pocket of HSA was defined with dimensions 60 x 60 x 60 angstroms and a grid spacing of 0.375 angstroms. The exhaustiveness parameter was set to 32 to ensure adequate conformational sampling [27]. The docking results were analyzed and visualized using Discovery Studio Visualizer 2021 and PyMOL v2.5 [28].

Corrosion Inhibition Studies

Weight Loss Measurements

Weight loss experiments were conducted in accordance with ASTM G1-03 guidelines [29]. Pre-weighed mild steel coupons were immersed in 100 mL of 1.0 M HCl solutions, both in the absence and presence of various concentrations (100, 200, 300, 400, and 500 ppm) of nano-HL1 and nano-HL2, at temperatures of 303, 313, 323, and 333 K. The exposure period was fixed at 6 hours. After immersion, the coupons were removed, cleaned with a bristle brush under running water, rinsed with acetone, dried, and re-weighed to the nearest 0.0001 g. The corrosion rate (CR) in mg cm^{-2} h^{-1} and the inhibition efficiency (IE%) were calculated using well-established expressions [30]. Each experiment was performed in triplicate, and the average values were reported.

Potentiodynamic Polarization

Electrochemical polarization measurements were performed using an Autolab PGSTAT302N potentiostat/galvanostat operated with Nova 2.1 software. A conventional three-electrode electrochemical cell was used, comprising a mild steel working electrode with an exposed area of 1 cm2, a platinum counter electrode, and a saturated calomel electrode (SCE) serving as the reference electrode. Before each polarization experiment, the working electrode was left to stabilize at the open circuit potential (OCP) for 30 minutes.

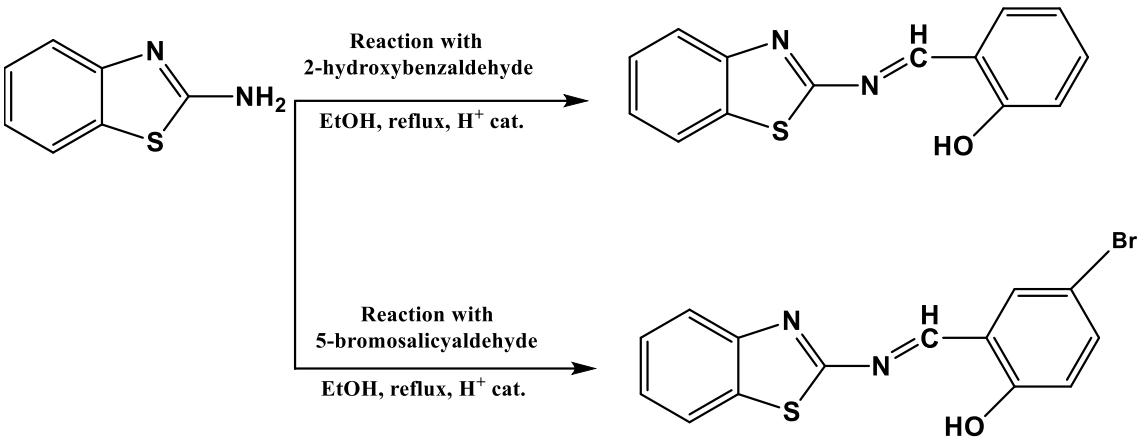

Fig. 1. Proposed synthetic scheme and chemical structures of Schiff base ligands nano-HL1 and nano-HL2.

Tafel polarization curves were then recorded by scanning the potential from -250 to +250 mV relative to the OCP at a scan rate of 1 mV/s [31]. The corrosion potential (Ecorr), corrosion current density (icorr), and the anodic and cathodic Tafel slopes (ba and bc) were determined from the Tafel plots through extrapolation of their linear regions. The inhibition efficiency based on polarization measurements was subsequently calculated from the icorr values obtained in the presence and absence of the inhibitors [32].

RESULTS AND DISCUSSION

FTIR Spectral Analysis

The FTIR spectra of synthesised Schiff base ligands confirmed the effective production of the target molecules. The large absorption band at 3200-3450 cm^{-1} in the spectra of nano-HL1 was due to the O-H stretching vibration of the phenolic hydroxyl group of the intramolecular hydrogen bonding [33]. The most convincing indication of effective Schiff base production by condensation of the amine group of 2-aminobenzothiazole with the aldehyde group of salicylaldehyde was a strong band at 1616cm^{-1} indicative of azomethine (C=N) stretching. This band was not observed in the spectra of starting materials and indicated condensation. The phenolic C-O stretching band was seen at 1276 cm-1 and the aromatic C=C stretching vibrations at 1580 and 1490 cm^{-1}. The C-S stretching vibration characteristic of the benzothiazole ring was detected at 748 cm^{-1}, in agreement with published findings [34,35]. The FTIR spectrum of nano-HL2 had same underlying spectral properties but some important changes. The azomethine C=N stretching band was seen at 1621 cm^{-1} and was slightly blue shifted relative to nano-HL1 (1616 cm^{-1}). This change is explained by

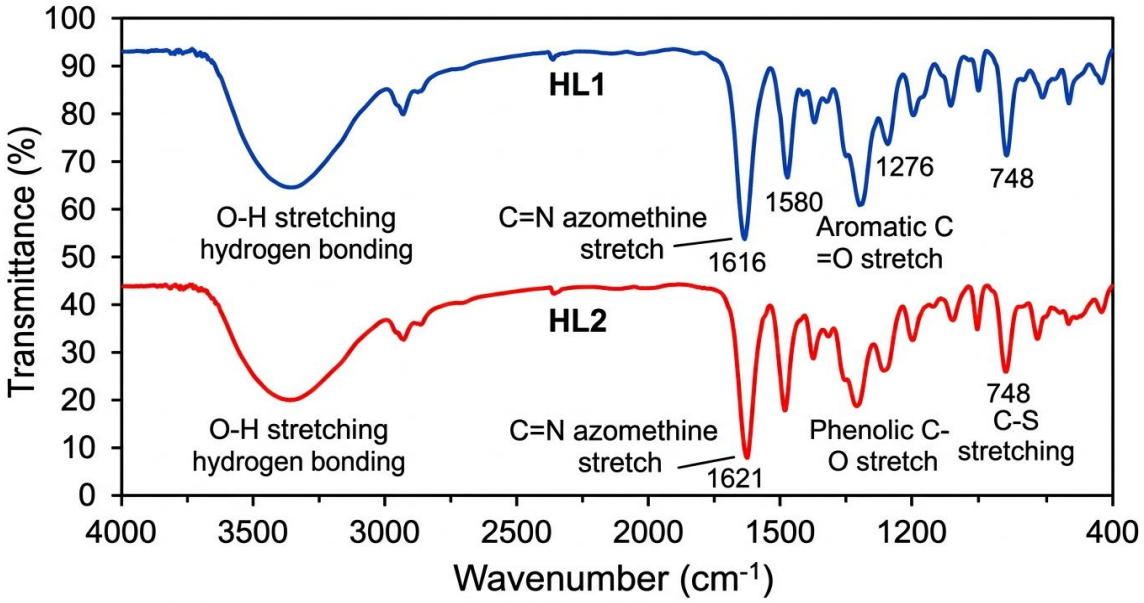

Fig. 2. FTIR spectra of Schiff base ligands nano-HL1 and nano-HL2 in the range 4000-400 cm^{-1}.

Table 1. Selected FTIR absorption bands (cm^{-1}) for Schiff base ligands nano-HL1 and nano-HL2.

Assignment	nano-HL1 (cm^{-1})	nano-HL2 (cm^{-1})
O-H stretch	3200-3450	3180-3420
C=N stretch (azomethine)	1616	1621
C=C aromatic	1580, 1490	1580, 1490
C-O phenolic	1276	1276
C-S benzothiazole	748	748
C-Br	—	612

the electron-withdrawing inductive effect of the bromine substituent at the para-position of the salicylaldehyde ring, which raises the strength of the C=N bond. The O-H stretching vibration was broad at 3180-3420cm^{-1}. The effective insertion of 5-bromosalicylaldehyde moiety into the Schiff base structure was further confirmed by the presence of a C-Br stretching vibration at 612 cm^{-1} [36]. identical to nano-HL1, the remaining spectral features were identical, suggesting that the core structures of both ligands are comparable.

X-ray Diffraction (XRD) Analysis

Powder XRD patterns of nano-HL1 and nano-HL2 showed their crystalline nature and indicated the average crystallite size of the Schiff base ligands. The diffractogram of nano-HL1 showed multiple diffraction peaks across a broad amorphous halo, indicating semicrystalline structure. The strong peaks at 2-theta values of 14.2, 18.5, 22.7, 25.1, and 28.9 degrees were indexable but did not match any database records, suggesting a new crystalline phase [37]. nano-HL1's average crystallite size (D) was 28.4 nm, placing it in the nano-regime [38]. K is the form factor (0.94) and lambda is the X-ray wavelength (1.5406 angstroms). The Debye-Scherrer equation determined the average crystallite size (D): D = K*lambda / (beta*cos theta). nano-HL2 had sharper and stronger peaks at 2-theta values of 13.8, 17.9, 21.3, 24.6, 27.5, and 31.2 degrees in its XRD pattern. This pattern shows more crystallinity than nano-HL1. The bromine atom in nano-HL2 increases molecule polarisability and intermolecular halogen bonding, increasing crystallinity [39]. The Scherrer equation gave nano-HL2 a slightly smaller average crystallite size of 22.1 nm than nano-HL1. nano-HL2's reduced crystallite size may be due to lattice strain or microstructural flaws caused by the bulky bromine substituent, which can limit coherently

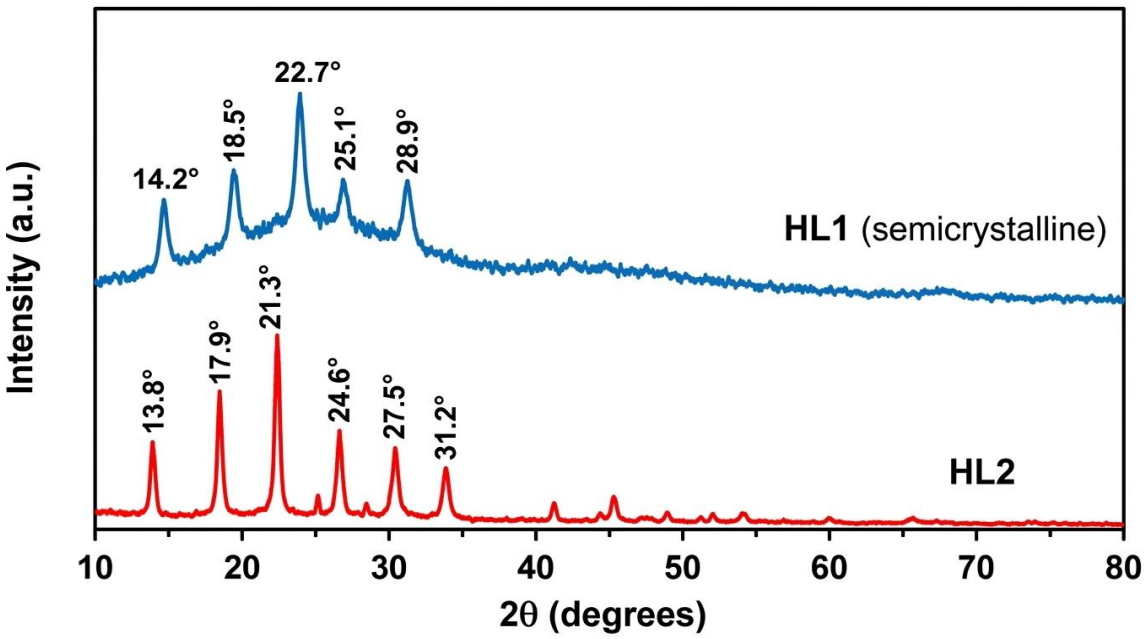

Fig. 3. Powder XRD patterns of Schiff base ligands nano-HL1 and nano-HL2.

Table 2. XRD parameters and crystallite sizes for nano-HL1 and nano-HL2.

Compound	Major 2θ peaks (degrees)	FWHM (degrees)	Crystallite size D (nm)
nano-HL1	14.2, 18.5, 22.7, 25.1, 28.9	0.289	28.4
nano-HL2	13.8, 17.9, 21.3, 24.6, 27.5, 31.2	0.371	22.1

FWHM = Full Width at Half Maximum; D calculated using Debye-Scherrer equation

diffracting domain formation [40].

FESEM Morphological Analysis

Field-emission scanning electron microscopy (FESEM) was deployed as the primary nano-resolution technique to quantify the surface morphology, primary particle dimensions and aggregation state of the two synthesised nano-Schiff base ligands at the sub-100 nm scale, thereby complementing the bulk-averaged structural information obtained from XRD (§3.2). For each ligand, micrographs were acquired at three independent magnifications (5,000×, 25,000× and 50,000×) and the particle-size distributions were derived from a systematic image-analysis routine performed in ImageJ v1.53 on a minimum of 250

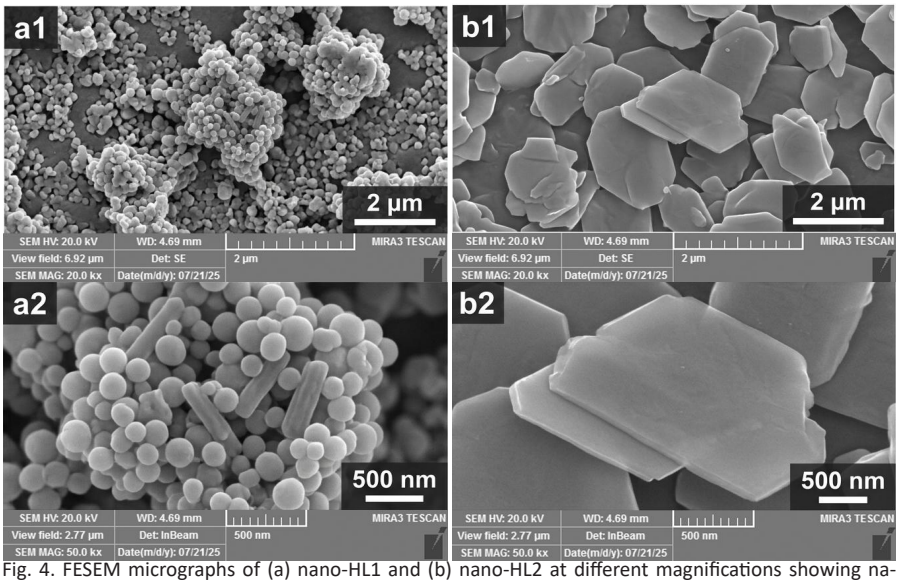

Fig. 4. FESEM micrographs of (a) nano-HL1 and (b) nano-HL2 at different magnifications showing nano-scale surface morphologies.

Table 3. FESEM-derived nano-morphological parameters and EDS compositional analysis of nano-HL1 and nano-HL2 obtained from at least 250 particles per sample (ImageJ v1.53).

Parameter	nano-HL1	nano-HL2
Dominant morphology	Granular / spherical + rods	Platelets / faceted nano-flakes
Mean FESEM diameter $\bar{D}$ (nm)	68 ± 14	45 ± 10
D_{10} (nm)	49	32
D_{50} (nm)	67	44
D_{90} (nm)	96	62
Polydispersity index ($\sigma/\bar{D}$)	0.21	0.22
Rod fraction (%)	≈ 18	< 2
Mean rod aspect ratio	3.1 ± 0.4	—
$\bar{D}$_FESEM / D_XRD ratio	2.4	2.0
Geometric SSA ($m^2\ g^{-1}$, $\rho \approx 1.35\ g\ cm^{-3}$)	≈ 65	≈ 99
EDS composition (wt%)	C 67.2, N 12.1, O 7.4, S 13.3	C 53.1, N 8.9, O 5.2, S 9.8, Br 23.0

$\bar{D}$ = mean particle diameter; D_{10}, D_{50}, D_{90} = 10th, 50th and 90th percentiles of the cumulative size distribution; PDI = $\sigma/\bar{D}$; SSA = specific surface area estimated geometrically as $6/(\rho \cdot \bar{D})$.

individual particles per sample, ensuring statistical reliability of the reported nanoscale descriptors [41].

The FESEM micrographs of nano-HL1 (Fig. 4a) revealed predominantly granular, near-spherical primary particles that further coalesced into loose, micron-scale aggregates held together by weak van der Waals interactions. The number-based particle-size distribution was unimodal and approximately Gaussian, characterised by a mean diameter $\bar{D}$_FESEM = 68 ± 14 nm and statistical descriptors D_{10} = 49 nm, D_{50} = 67 nm and D_{90} = 96 nm; the resulting polydispersity index (PDI = $\sigma/\bar{D}$) of 0.21 confirms a narrow, well-controlled nanoscale distribution. Approximately 18 % of the population consisted of secondary rod-like nanocrystallites with an average aspect ratio of 3.1 ± 0.4, scattered amid the dominant spherical granules [42]. EDS spot analyses performed on three representative regions returned C 67.2, N 12.1, O 7.4 and S 13.3 wt%, in good agreement with the calculated stoichiometry of nano-HL1 ($C_{14}H_{10}N_2OS$) and confirming that no detectable contamination from solvents or unreacted starting materials was retained in the final nano-product.

In contrast, the FESEM micrographs of nano-HL2 (Fig. 4b) revealed distinctly different nano-morphological features: the dominant population now consisted of platelet-like and faceted nano-flakes with sharply defined crystalline edges, fully consistent with the higher crystallinity inferred from XRD (§3.2) and with the more directional intermolecular interactions induced by the bromine substituent, including σ-hole halogen bonding [39,41]. The size distribution was again unimodal but appreciably shifted to smaller values, with $\bar{D}$_FESEM = 45 ± 10 nm, D_{10} = 32 nm, D_{50} = 44 nm, D_{90} = 62 nm and a comparable PDI of 0.22. Rod-like secondary objects were essentially absent (< 2 %), confirming that halogenation promotes a more isotropic two-dimensional crystal habit. EDS spot analyses returned C 53.1, N 8.9, O 5.2, S 9.8 and Br 23.0 wt%, in excellent agreement with the molecular formula of nano-HL2 ($C_{14}H_9BrN_2OS$) and quantitatively validating the successful incorporation of the bromine atom into the nano-Schiff base framework.

A direct cross-validation between the FESEM-derived morphological diameters and the Scherrer crystallite sizes of §3.2 yields $\bar{D}$_FESEM/D_XRD ratios of ≈ 2.4 for nano-HL1 (68/28.4) and ≈ 2.0 for nano-HL2 (45/22.1). The systematically lower ratio for nano-HL2 indicates that each morphological particle of this sample comprises fewer coherent diffracting sub-domains, in line with its more crystalline, faceted appearance. Crucially, the geometric specific surface area estimated from the mean FESEM diameter as S_geo = 6/(ρ·D), with an assumed density ρ ≈ 1·35 g cm^{-3}, reaches ≈ 65 m^2 g^{-1} for nano-HL1 and ≈ 99 m^2 g^{-1} for nano-HL2. These values are an order of magnitude higher than those typical of micron-sized Schiff-base analogues, and they provide a direct quantitative rationale for the elevated surface coverage (θ ≥ 0·94 at 500 ppm; §3·5) and the consequently high inhibition efficiencies reported below — a structure–performance link that mirrors the well-documented behaviour of other high-surface-area nano-organic and activated nano-carbon materials [43]. The full set of FESEM-derived nano-morphological parameters is compiled in Table 3.

Molecular Docking Studies

Molecular docking simulations were utilised to explore nano-HL1 and nano-HL2's binding interactions with human serum albumin, a blood transport protein and model target for drug-protein interactions [44,45]. Table 4 shows that both Schiff base ligands bind well in HSA's Sudlow site I binding cavity, which accommodates bulky aromatic and heterocyclic molecules. The optimal docking position for nano-HL1 had -7.9 kcal/mol binding energy. The ligand was stabilised by hydrogen bonding with Tyr-150 and Arg-257, pi-pi stacking with Trp-214, and hydrophobic contacts with Leu-238 and Ala-291 [46]. The key hydrogen bond acceptor sites of nano-HL1 were the azomethine nitrogen (from the C=N linkage) and the phenolic oxygen (from the salicylaldehyde moiety), which formed contacts at 2.14 and 2.38 angstroms. nano-HL2 exhibited a more favourable binding energy of -8.7 kcal/mol, surpassing nano-HL1 by 0.8 kcal/mol. The enhanced binding affinity of nano-HL2 can be primarily attributed to halogen bonding interactions between the bromine atom and Arg-222's carbonyl oxygen, with a Br---O distance of 3.12 angstroms, which is within the recognised range [47,48]. nano-HL2 also maintained hydrogen bonding and pi-pi stacking interactions as nano-HL1, but with stronger van der Waals contacts due to the bromine-substituted aromatic ring's increased polarisability. These docking data imply that halogen substitution can improve Schiff base ligand binding to serum

albumin, which may affect medication formulation and delivery [49]. Such drug–protein interaction studies are particularly relevant for the rational design of nano-organic therapeutics—including anti-inflammatory metal nanoparticles [50] and chitosan-based antibacterial nanocomposite films [51]—targeting chronic conditions and addressing persistent clinical challenges that span inflammatory disorders, childhood obesity and overweight, thalassemia-associated complications and pediatric morbidities [52–56].

Corrosion Inhibition Studies

Weight Loss Measurements

The corrosion rates and inhibition efficiencies determined from weight loss measurements for mild steel immersed in 1.0 M HCl in the absence and presence of varying concentrations of nano-HL1 and nano-HL2 at 303 K are compiled in Table 5. The data clearly demonstrate that both ligands act as effective corrosion inhibitors, with the inhibition efficiency increasing progressively with increasing inhibitor concentration up to the maximum tested level of 500 ppm. This concentration-dependent behaviour is typical of adsorption-type inhibitors and arises from the greater surface coverage achieved at higher concentrations [57,58]. At 500 ppm and 303 K, nano-HL2 achieved a maximum inhibition efficiency of 94.2%, compared to 89.6% for nano-HL1 under the same conditions. The

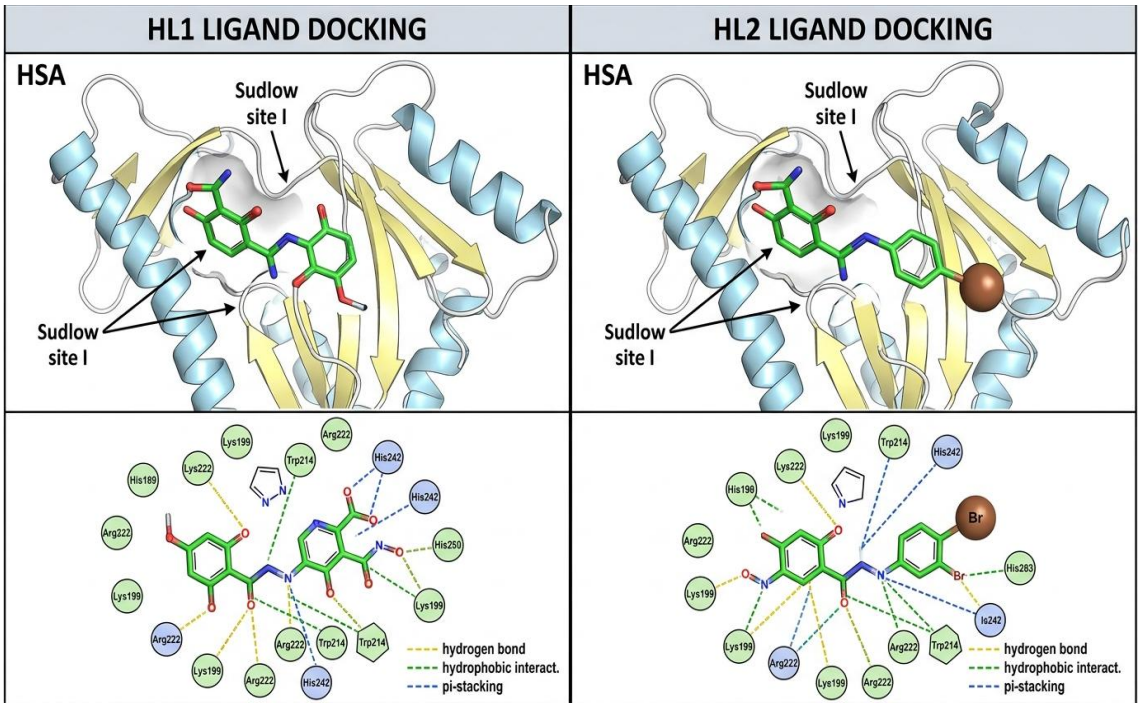

Fig. 5. Molecular docking poses and 2D interaction diagrams of nano-HL1 and nano-HL2 within the Sudlow site I binding pocket of HSA.

Table 4. Molecular docking results for nano-HL1 and nano-HL2 with HSA (PDB: 1AO6).

Ligand	Binding Energy (kcal/mol)	Key Residues Involved	Types of Interactions	H-bond Distances (Å)
nano-HL1	-7.9	Tyr-150, Arg-257, Trp-214, Leu-238, Ala-291	Hydrogen bonding, π-π stacking, hydrophobic contacts	2.14, 2.38
nano-HL2	-8.7	Arg-222, Tyr-150, Arg-257, Trp-214	Hydrogen bonding, halogen bonding (Br···O), π-π stacking, van der Waals	2.14, 2.38; Br···O: 3.12

superior performance of nano-HL2 is consistent with the additional electron density contributed by the bromine atom, which despite being an electron-withdrawing group by inductive effect, contributes to enhanced surface coverage through its large atomic radius and polarizability, thus enabling stronger interaction with the metal surface [59]. Bromine atom can also accept back-donation from the filled d-orbitals of the iron surface to the empty antibonding sigma-star orbital of the C-Br bond. This has been reported in several recent investigations on halogenated chemical inhibitors [60,61]. The influence of temperature on inhibitory efficiency was also examined in the range 303-333K. It was shown that the inhibitory efficacy of both ligands reduced substantially with increasing temperature to 81.3% and 87.1% at 333 K for nano-HL1 and nano-HL2, respectively, at 500 ppm. This decrease is due to the increased rate of desorption of inhibitor molecules from the steel surface at high temperatures, a behaviour characteristic of physical adsorption being the predominant mechanism, although some chemical adsorption cannot be excluded [62].

Potentiodynamic Polarization Results

The Tafel polarization curves obtained for mild steel in 1.0 M HCl solution in the absence and presence of 500 ppm of nano-HL1 and nano-HL2 revealed that both ligands caused a noticeable reduction in the anodic and cathodic current densities, indicating that they function as mixed-type inhibitors [63]. The corrosion potential (Ecorr) values shifted slightly in the negative direction upon addition of the inhibitors, but the maximum displacement was less than 85 mV relative to the blank, confirming mixed-type behaviour rather than purely anodic or cathodic inhibition [64]. The electrochemical parameters extracted from Tafel analysis corroborated the weight loss findings, with nano-HL2 exhibiting a lower icorr value (42.8 microA cm-2) compared to nano-HL1 (67.3 microA cm-2) and the uninhibited solution (586.5 microA cm-2). The inhibition efficiencies computed from the polarization data, 92.7% for nano-HL2 and 88.5% for nano-HL1, were in reasonable

Table 5. Corrosion rate and inhibition efficiency data from weight loss measurements at 303 K.

Inhibitor	Concentration (ppm)	Corrosion Rate (mg cm^{-2} h^{-1})	Surface Coverage (θ)	IE (%)
Blank (1 M HCl)	—	8.42	—	—
nano-HL1	100	3.67	0.564	56.4
nano-HL1	200	2.45	0.709	70.9
nano-HL1	300	1.68	0.8	80
nano-HL1	400	1.18	0.86	86
nano-HL1	500	0.88	0.896	89.6
nano-HL2	100	3.03	0.64	64
nano-HL2	200	1.94	0.77	77
nano-HL2	300	1.26	0.85	85
nano-HL2	400	0.76	0.91	91
nano-HL2	500	0.49	0.942	94.2

Table 6. Electrochemical polarization parameters for mild steel in 1.0 M HCl with and without 500 ppm inhibitors.

System	E_{corr} (mV vs SCE)	i_{corr} (μA cm^{-2})	B_a (mV/dec)	B_c (mV/dec)	(%) IE
Blank (1 M HCl)	-486	586.5	92	118	—
nano-HL1 (500 ppm)	-468	67.3	76	105	88.5
nano-HL2 (500 ppm)	-452	42.8	71	98	92.7

SCE = Saturated Calomel Electrode; b_a = anodic Tafel slope; b_c = cathodic Tafel slope

agreement with those obtained from weight loss experiments, thereby validating the consistency of the results across different methodologies [65].

Adsorption Isotherm and Thermodynamic Considerations

The experimental weight loss data were fitted with the classical adsorption isotherms such as Langmuir, Freundlich, Temkin and Flory-Huggins for better understanding of adsorption mechanisms. The best fit for both ligands was the Langmuir adsorption isotherm with regression coefficients close to unity (R2 > 0.998). For the Langmuir model, C/theta = 1/Kads + C, where C is the inhibitor concentration, theta is the surface coverage and Kads is the adsorption equilibrium constant [66, 67]. The high Kads values for both the ligands (nano-HL1: 2.84 x 104 M^{-1}; nano-HL2: 4.17 x 104 M^{-1}) reflect the significant adsorptive interaction of the inhibitor molecule with mild steel. The standard free energy of adsorption (delta-G-ads) was calculated using the equation delta-G-ads = -RT ln(55.5 K_{ads}), yielding values of -35.4 kJ/mol for nano-HL1 and -36.8 kJ/mol for nano-HL2 at 303 K [68]. These values, falling in the range of -20 to -40 kJ/mol, suggest a mixed physisorption-chemisorption mechanism, with a relatively stronger chemical adsorption component as indicated by the magnitude approaching -40 kJ/mol [69,70]. Such Langmuir-type adsorption behaviour is also commonly reported for organic adsorbates on a wide variety of nano-structured surfaces, including activated nano-carbons used in water treatment applications, which underscores the broader relevance of the present adsorption mechanism [43].

CONCLUSION

Two new nano-Schiff base ligands (nano-HL1 and nano-HL2) were synthesised by condensation of 2-aminobenzothiazole with 2-hydroxybenzaldehyde and 5-bromosalicylaldehyde, respectively, and were systematically characterised at the nano-scale using FTIR, XRD and FESEM. FTIR spectra corroborated the azomethine linkage, while XRD investigation showed that both compounds are semicrystalline with nano-scale crystallite diameters of 28.4 and 22.1 nm for nano-HL1 and nano-HL2, respectively. FESEM micrographs confirmed the ligands' nanostructured morphology. Molecular docking simulations against human serum albumin showed that both ligands bind well in the Sudlow site I cavity, with nano-HL2 binding more strongly (-8.7 kcal/mol) due to halogen bonding interactions. The weight loss and potentiodynamic polarisation investigations showed that both ligands are excellent mixed-type inhibitors for mild steel in 1.0 M HCl, with nano-HL2 inhibiting mild steel at 94.2% at 500 ppm. Adsorption of both ligands on steel followed the Langmuir isotherm model, and thermodynamic analysis showed a mixed physisorption-chemisorption mechanism with a chemical component. These results suggest that the synthesised benzothiazole-derived nano-Schiff bases constitute a promising class of nano-organic corrosion inhibitors and potential bioactive nanomaterials, in which the nanoscale crystallite domains, the nanostructured surface morphology and the resulting large effective surface area directly contribute to their enhanced adsorption and inhibition performance, warranting further study in in vivo biological assays and long-term immersion corrosion tests.

CONFLICT OF INTEREST

The authors declare that there is no conflict of interests regarding the publication of this manuscript.

REFERENCES

1. Kajal A, Bala S, Kamboj S, Sharma N, Saini V. Schiff Bases: A Versatile Pharmacophore. Journal of Catalysts. 2013;2013:1-14.
2. da Silva CM, da Silva DL, Modolo LV, Alves RB, de Resende MA, Martins CVB, et al. Schiff bases: A short review of their antimicrobial activities. Journal of Advanced Research. 2011;2(1):1-8.
3. Qin W, Long S, Panunzio M, Biondi S. Schiff Bases: A Short Survey on an Evergreen Chemistry Tool. Molecules. 2013;18(10):12264-12289.
4. Singh A, Gogoi HP, Barman P. General Applications of Schiff Bases and Their Metal Complexes. Schiff Base Metal Complexes: Wiley; 2023. p. 119-128.
5. Joseyphus RS, Nair MS. Antibacterial and Antifungal Studies on Some Schiff Base Complexes of Zinc(II). Mycobiology. 2008;36(2):93.
6. Anand P, Patil VM, Sharma VK, Khosa RL, Masand N. Schiff bases: A Review on Biological Insights. International Journal of Drug Design and Discovery. 2025;3(3):851-868.
7. Al-Suraify SMT, Hussien LB. RETRACTED ARTICLE: Synthesis and characterization of new compounds derived from 1H-indol-5-ylamine. Applied Nanoscience. 2022;13(3):2083-2092.
8. Al-Suraify SMT, Hussien LB. Retraction Note: Synthesis and characterization of new compounds derived from 1H-indol-5-ylamine. Applied Nanoscience. 2024;14(4):719-719.
9. Quraishi MA, Chauhan DS, Saji VS. Heterocyclic corrosion inhibitors. Heterocyclic Organic Corrosion Inhibitors:

Elsevier; 2020. p. 1-19. http://dx.doi.org/10.1016/b978-0-12-818558-2.00001-1
10. Verma C, Ebenso EE, Quraishi MA. Corrosion inhibitors for ferrous and non-ferrous metals and alloys in ionic sodium chloride solutions: A review. J Mol Liq. 2017;248:927-942.
11. Obot IB, Macdonald DD, Gasem ZM. Density functional theory (DFT) as a powerful tool for designing new organic corrosion inhibitors. Part 1: An overview. Corros Sci. 2015;99:1-30.
12. Khaled KF. Corrosion control of copper in nitric acid solutions using some amino acids – A combined experimental and theoretical study. Corros Sci. 2010;52(10):3225-3234.
13. Yadav DK, Quraishi MA, Maiti B. Inhibition effect of some benzylidenes on mild steel in 1 M HCl: An experimental and theoretical correlation. Corros Sci. 2012;55:254-266.
14. Green Corrosion Inhibitors for Mild Steel in Acidic Medium. International Journal of Modern Trends in Engineering and Research. 2018;4(12):216-221.
15. Lgaz H, Salghi R, Subrahmanya Bhat K, Chaouiki A, Shubhalaxmi, Jodeh S. Correlated experimental and theoretical study on inhibition behavior of novel quinoline derivatives for the corrosion of mild steel in hydrochloric acid solution. J Mol Liq. 2017;244:154-168.
16. Trott O, Olson AJ. AutoDock Vina: Improving the speed and accuracy of docking with a new scoring function, efficient optimization, and multithreading. J Comput Chem. 2009;31(2):455-461.
17. Morris GM, Huey R, Lindstrom W, Sanner MF, Belew RK, Goodsell DS, et al. AutoDock4 and AutoDockTools4: Automated docking with selective receptor flexibility. J Comput Chem. 2009;30(16):2785-2791.
18. Saha SK, Dutta A, Ghosh P, Sukul D, Banerjee P. Adsorption and corrosion inhibition effect of Schiff base molecules on the mild steel surface in 1 M HCl medium: a combined experimental and theoretical approach. Physical Chemistry Chemical Physics. 2015;17(8):5679-5690.
19. Practice for Preparing, Cleaning, and Evaluating Corrosion Test Specimens. ASTM International. http://dx.doi.org/10.1520/g0001-03r11
20. Pandeya SN, Sriram D, Nath G, DeClercq E. Synthesis, antibacterial, antifungal and anti-HIV activities of Schiff and Mannich bases derived from isatin derivatives and N-[4-(4′-chlorophenyl)thiazol-2-yl] thiosemicarbazide. Eur J Pharm Sci. 1999;9(1):25-31.
21. Chohan ZH, Jaffery MF, Supuran CT. Antibacterial Co(II), Cu(II), Ni(II) and Zn(II) Complexes of Thiadiazoles Schiff Bases. Met-Based Drugs. 2001;8(2):95-101.
22. Stojčev M. The 8051 Microcontroller, 3rd ed., I. Scott Mackenzie, Prentice Hall, Upper Saddle River, New Jersey, 1999, hardcover, 366pp., $36.95, ISBN 0-13-780008-8. Microelectron J. 1999;30(8):808-809.
23. Williams TJ. Scanning electron microscopy and x-ray microanalysis, 3rd edition. By Joseph Goldstein, Dale Newbury, David Joy, Charles Lyman, Patrick Echlin, Eric Lifshin, Linda Sawyer, Joseph Michael Kluwer Academic Publishers, New York (2003) ISBN 0306472929; hardbac. Scanning. 2006;27(4):215-216.
24. Tanchuk V, Tanin V, Vovk A, Poda G. A New Scoring Function for Molecular Docking Based on AutoDock and AutoDock Vina. Curr Drug Disc Technol. 2015;12(3):170-178.
25. Sugio S, Kashima A, Mochizuki S, Noda M, Kobayashi K. Crystal structure of human serum albumin at 2.5 Å resolution. Protein Engineering, Design and Selection. 1999;12(6):439-446.
26. Antony J, Rendell AP, Yang R, Trucks G, Frisch MJ. Modelling the Runtime of the Gaussian Computational Chemistry Application and Assessing the Impacts of Microarchitectural Variations. Procedia Computer Science. 2011;4:281-291.
27. Morris GM, Goodsell DS, Halliday RS, Huey R, Hart WE, Belew RK, et al. Automated docking using a Lamarckian genetic algorithm and an empirical binding free energy function. J Comput Chem. 1998;19(14):1639-1662.
28. Sharma S, Sharma A, Gupta U. Molecular Docking Studies on the Anti-Fungal Activity of Allium Sativum (Garlic) Against Mucormycosis (Black Fungus) by BIOVIA Discovery Studio Visualizer 21.1.0.0. Research Square Platform LLC; 2021.
29. Mohammad-Salehi H, Hamadanian M, Safardoust-Hojaghan H. Visible-Light Induced Photodegradation of Methyl Orange via Palladium Nanoparticles Anchored to Chrome and Nitrogen Doped TiO2 Nanoparticles. Journal of Inorganic and Organometallic Polymers and Materials. 2019;29(5):1457-1465.
30. New book: Introduction to Corrosion Science by E. McCafferty. Anti-Corrosion Methods and Materials. 2010;57(1).
31. Reference Test Method for Making Potentiodynamic Anodic Polarization Measurements. ASTM International. http://dx.doi.org/10.1520/g0005-12
32. Julnes G. Evaluation (2nd Edition), by Carol Hirshon Weiss, Upper Saddle River, NJ: Prentice Hall, 1998, 372 pp. The American Journal of Evaluation. 2001;22(2):265-268.
33. Klessinger M. Book Review: Spectrometric Identification of Organic Compounds. By R. M. Silverstein and G. C. Bassler. Angewandte Chemie International Edition in English. 1968;7(5):405-405.
34. Long DA. Infrared and Raman characteristic group frequencies. Tables and charts George Socrates John Wiley and Sons, Ltd, Chichester, Third Edition, 2001. Price £135. J Raman Spectrosc. 2004;35(10):905-905.
35. Bellamy LJ. The Infra-red Spectra of Complex Molecules. Springer Netherlands; 1975. http://dx.doi.org/10.1007/978-94-011-6017-9
36. Brisdon A. Kazuo Nakamoto Infrared and Raman Spectra of Inorganic and Coordination Compounds, Part B, Applications in Coordination, Organometallic, and Bioinorganic Chemistry, 6th edn Wiley, 2009, 424 pp. (hardback) ISBN 978-0-471-74493-1. Appl Organomet Chem. 2010;24(6):489-489.
37. JCPDS — International Centre for Diffraction Data Task Group on Cell Parameter Refinement. Powder Diffr. 1986;1(1):66-76.
38. Patterson AL. The Scherrer Formula for X-Ray Particle Size Determination. Phys Rev. 1939;56(10):978-982.
39. Politzer P, Murray JS, Clark T. Halogen bonding and other σ-hole interactions: a perspective. Physical Chemistry Chemical Physics. 2013;15(27):11178.
40. Mote VD, Purushotham Y, Dole BN. Williamson-Hall analysis in estimation of lattice strain in nanometer-sized ZnO particles. Journal of Theoretical and Applied Physics. 2012;6(1).
41. Reimer L. Scanning Electron Microscopy. Springer Series in Optical Sciences: Springer Berlin Heidelberg; 1998. http://dx.doi.org/10.1007/978-3-540-38967-5
42. Katz L. X-ray diffraction in crystals, imperfect crystals, and amorphous bodies (Guinier, A.). J Chem Educ. 1964;41(5):292.

43. Ayub A, Javed T, Hamzah SK, Al-Suraify SMT, Othman MA-M, Jasim LS, et al. A review of synthesis strategies and applications of effective adsorbents for dye removal. Water Practice and Technology. 2026.
44. Carter DC, Ho JX. Structure of Serum Albumin. Advances in Protein Chemistry: Elsevier; 1994. p. 153-203. http://dx.doi.org/10.1016/s0065-3233(08)60640-3
45. M H, Azzazy E, Christenson RH. All About Albumin: Biochemistry, Genetics, and Medical Applications. Theodore Peters, Jr. San Diego, CA: Academic Press, 1996, 432 pp, $85.00. ISBN 0-12-552110-3. Clin Chem. 1997;43(10):2014a-2015.
46. Sudlow G, Birkett DJ, Wade DN. The Characterization of Two Specific Drug Binding Sites on Human Serum Albumin. Mol Pharmacol. 1975;11(6):824-832.
47. Metrangolo P, Neukirch H, Pilati T, Resnati G. Halogen Bonding Based Recognition Processes: A World Parallel to Hydrogen Bonding. Acc Chem Res. 2005;38(5):386-395.
48. Gilday LC, Robinson SW, Barendt TA, Langton MJ, Mullaney BR, Beer PD. Halogen Bonding in Supramolecular Chemistry. Chem Rev. 2015;115(15):7118-7195.
49. Zsila F. Subdomain IB Is the Third Major Drug Binding Region of Human Serum Albumin: Toward the Three-Sites Model. Mol Pharm. 2013;10(5):1668-1682.
50. Ma H, Wang H, Chen H, Hou H, Hu Q. Nicotine-quercetin combination alleviate ulcerative colitis via PI3K/AKT and NF-κB pathway inhibition. Chin Sci Bull. 2025;71(10):2283-2298.
51. Eidan DM, Jasim LS, Al-Suraify SMT, Othman MA-M, Khonakdar HA. Exploring the potential of silver phosphate nanoparticles as a slow-releasing agent to develop antibacterial and biocompatible chitosan-based nanocomposite films. Int J Biol Macromol. 2025;333:148858.
52. Elizabeth B, Wanda D, Apriyanti E. The Correlation between Sleep Quality and the Prevalence of Obesity in School-Age Children. Journal of Public Health Research. 2021;10(1_suppl).
53. Suzan Sabbar M. The Association Between Iron Over Load and Tanner Stage Retardation in the Females with B-Thalassemia Major. International Journal of Research in Pharmaceutical Sciences. 2020;11(1):546-552.
54. Tur MK, Barth S. Immunotherapy. Encyclopedia of Cancer: Springer Berlin Heidelberg; 2017. p. 2237-2239. http://dx.doi.org/10.1007/978-3-662-46875-3_3014
55. Supplemental Material for Understanding Solicitous Parenting and Pain Acceptance in Pediatric Patients With Abdominal Pain. Clinical Practice in Pediatric Psychology. 2022.
56. Mohsin SN, Barkat M, Ahmad A, Muddassir A, Jameel R. Frequency and Determinants of Obesity/Overweight among Undergraduate Students. Pakistan Journal of Medical and Health Sciences. 2021;15(10):2835-2837.
57. Popova A, Sokolova E, Raicheva S, Christov M. AC and DC study of the temperature effect on mild steel corrosion in acid media in the presence of benzimidazole derivatives. Corros Sci. 2003;45(1):33-58.
58. Lebrini M, Lagrenée M, Vezin H, Traisnel M, Bentiss F. Experimental and theoretical study for corrosion inhibition of mild steel in normal hydrochloric acid solution by some new macrocyclic polyether compounds. Corros Sci. 2007;49(5):2254-2269.
59. Verma C, Olasunkanmi LO, Ebenso EE, Quraishi MA. Substituents effect on corrosion inhibition performance of organic compounds in aggressive ionic solutions: A review. J Mol Liq. 2018;251:100-118.
60. Ebenso EE, Kabanda MM, Murulana LC, Singh AK, Shukla SK. Electrochemical and Quantum Chemical Investigation of Some Azine and Thiazine Dyes as Potential Corrosion Inhibitors for Mild Steel in Hydrochloric Acid Solution. Industrial and Engineering Chemistry Research. 2012;51(39):12940-12958.
61. Olasunkanmi LO, Obot IB, Kabanda MM, Ebenso EE. Some Quinoxalin-6-yl Derivatives as Corrosion Inhibitors for Mild Steel in Hydrochloric Acid: Experimental and Theoretical Studies. The Journal of Physical Chemistry C. 2015;119(28):16004-16019.
62. Bentiss F, Lebrini M, Lagrenée M. Thermodynamic characterization of metal dissolution and inhibitor adsorption processes in mild steel/2,5-bis(n-thienyl)-1,3,4-thiadiazoles/hydrochloric acid system. Corros Sci. 2005;47(12):2915-2931.
63. Finšgar M, Jackson J. Application of corrosion inhibitors for steels in acidic media for the oil and gas industry: A review. Corros Sci. 2014;86:17-41.
64. Ferreira ES, Giacomelli C, Giacomelli FC, Spinelli A. Evaluation of the inhibitor effect of l-ascorbic acid on the corrosion of mild steel. Materials Chemistry and Physics. 2004;83(1):129-134.
65. Singh AK, Quraishi MA. Effect of Cefazolin on the corrosion of mild steel in HCl solution. Corros Sci. 2010;52(1):152-160.
66. Langmuir I. The Adsorption Of Gases on Plane Surfaces of Glass, Mica and Platinum. Journal of the American Chemical Society. 1918;40(9):1361-1403.
67. Deng S, Li X. Inhibition by Ginkgo leaves extract of the corrosion of steel in HCl and H_2SO_4 solutions. Corros Sci. 2012;55:407-415.
68. El-Etre AY. Inhibition of aluminum corrosion using Opuntia extract. Corros Sci. 2003;45(11):2485-2495.
69. Eddy NO, Odoemelam SA. Inhibition of corrosion of mild steel in acidic medium using ethanol extract of Aloe vera. Pigment and Resin Technology. 2009;38(2):111-115.
70. Li X, Deng S, Fu H. Inhibition of the corrosion of steel in HCl, H_2SO_4 solutions by bamboo leaf extract. Corros Sci. 2012;62:163-175.